Research of Vortex Identification Algorithm and Its Application to Aircraft Wake Flow Vortices

R Zhu[1], Z Y Chen[1], S Li[1], Y Q Tan[1], Y R Mo[1], F Bao[1] and Z R Liu[*]

Department of Power Engineering, School of Aerospace Engineering, Xiamen University, Xiamen 361005, China

Corresponding author and e-mail: Z R Liu, lzr1222@126.com

Abstract. Vortex identification is very critical for PIV (Particle Image Velocimetry) post-processing to obtain the precise vortex formation. The research focuses on studying & comparing several popular vortex identification methods which are based on velocity gradient tensor derived the second invariant Q, the characteristic equation discriminant Δ, the complex eigenvalue imaginary part λ_{ci} and the pressure second eigenvalue λ_2. By comparing and analyzing different vortex identification algorithms to detect the vortex region, the Δ criteria with the best display effect is applied to the aircraft vortex data of the four vortices system to study the influence of the initial vortex and the initial position of the vortex on the dissipation of the main vortex. The research results indicate that the higher small-vortex initial circulation will speed up primary vortex dissipation and the wake vortex strength may reach weakest as the small-vortex initial circulation is of an appropriate value. The closer the initial position of small-vortex to primary vortex will also speed up vortices interactions but non-linearly related to primary vortex dissipation, and if the distance is too close, it will cause the small vortex to be thrown off by the main vortex.

1. Introduction

The research on vortex is always frontier in fluid mechanics due to the vortex's unsteady, multidimensional & nonlinear complicated mechanism and its importance to engineering applications [1]. The PIV testing technology is essentially an image analysis technology. The speed field obtained by the PIV is only an intermediate product for studying the complex flow and needs further post-processing to extract important flow field information. In fact, some recent vortex identification criteria based on wavelet analysis have been proved to be very effective [2, 3]. The vortex identification algorithm for 2D PIV velocity field is deduced and programmed in Matlab in this paper. The vortex identification method for 3D velocity field is also deduced and programmed in Tecplot to be compared with 3D numerical experiments results. Applying optimal method to aircraft wake flow vortices to get precise vortex visualization, further understanding the vortex's formation, development & dissipation and vortices' interactions & control, then conversely improves and optimizes flow formations.

In the actual PIV measurement process, due to improper exposure of the collection device, uneven concentration of tracer particles, noise interference, etc., the peak value of the correlation function in the analysis process is likely to be indeterminate, resulting in spurious vectors in the velocity field.

The data obtained from the FMPL laboratory's Dynamic Studio software was used to confirm the data and replace the erroneous data. Finally, the initial data of vortex structure detection was obtained.

2. PIV experiments

According to experimental equipment performance and measurement requirements, the frequency of the high-frequency camera is set to 100 Hz, the image used for cross-correlation analysis is 1 608 pixels by 1 176 pixels, and the size of the Interrogation Window is 16 pixels by 16 pixels. The picture contains 134×98 data points. The laser is irradiated from the side of the sink and the laser cuts the vertical sink axis. The trailer drags the model along the axis of the sink. The PIV camera shoots at the end of the sink and records the development of the wake vortex on the laser cut surface. Set the trolley drag speed to 0.1m/s, and data was collected after the dragging model passed through the laser cut plane. Each set of experiments was collected for 10 seconds and a total of 1,000 original particle images were processed. Then the PIV software was used to process the images recorded by the camera to obtain the velocity vector field and vorticity field in the measurement area. In order to ensure the reliability of the experimental data, each group of PIV experiments was repeated twice.

In PIV experiments, two wing models with different sizes are used to generate primary vortex and secondary vortex (Figure 1). As water flows through two wing models the two wingtip vortices are created by airfoil's upper-lower surface pressure difference, the secondary vortex performs twisting motion around primary vortex due to primary vortex shear [4].
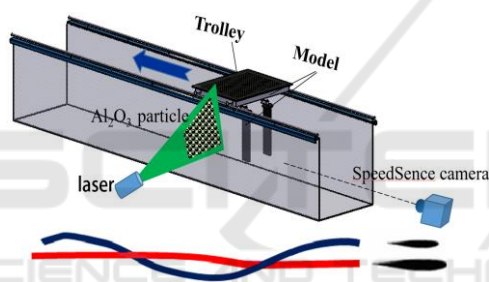

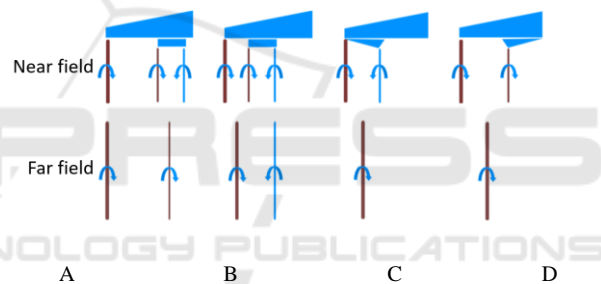**Figure 1.** Model installation.　　**Figure 2.** Vortices' interactions & transformations.

The trails of two vortices are presented in Figure 1, the red curve represents primary vortex trail and blue curve represents secondary vortex trail. Generally there are four types of vortices' interactions & transformations according to where the small vortex generated as shown in Figure 2, the thickness of line represents vortex strength. A, B, C are traditionally typical flap installations [5].

3. Vortex identification algorithm

If instantaneous streamlines are projected to plane which is vertical to vortex center and look like round or helix in relative reference system, this domain can be identified as vortex [6]. However, this definition is not applicable to pure-shear flow, so based on velocity gradient tensor the second invariant Q, the characteristic equation discriminant Δ, the complex eigenvalue imaginary part λ_{ci} and the pressure second eigenvalue λ_2 are proposed. These criteria have more accurate mathematical definition and physical interpretation, and can weaken the influence of shear flow on vortex identification.

3.1. Basic theory
Velocity gradient tensor ∇U is:

$$\nabla U = \begin{bmatrix} \dfrac{\partial U}{\partial x} & \dfrac{\partial V}{\partial x} & \dfrac{\partial W}{\partial x} \\[2mm] \dfrac{\partial U}{\partial y} & \dfrac{\partial V}{\partial y} & \dfrac{\partial W}{\partial y} \\[2mm] \dfrac{\partial U}{\partial z} & \dfrac{\partial V}{\partial z} & \dfrac{\partial W}{\partial z} \end{bmatrix} = \begin{bmatrix} \dfrac{\partial U}{\partial x} & \dfrac{1}{2}\left(\dfrac{\partial V}{\partial x}+\dfrac{\partial U}{\partial y}\right) & \dfrac{1}{2}\left(\dfrac{\partial W}{\partial x}+\dfrac{\partial U}{\partial z}\right) \\[2mm] \dfrac{1}{2}\left(\dfrac{\partial V}{\partial x}+\dfrac{\partial U}{\partial y}\right) & \dfrac{\partial V}{\partial y} & \dfrac{1}{2}\left(\dfrac{\partial W}{\partial y}+\dfrac{\partial V}{\partial z}\right) \\[2mm] \dfrac{1}{2}\left(\dfrac{\partial W}{\partial x}+\dfrac{\partial U}{\partial z}\right) & \dfrac{1}{2}\left(\dfrac{\partial W}{\partial y}+\dfrac{\partial V}{\partial z}\right) & \dfrac{\partial W}{\partial z} \end{bmatrix} + \begin{bmatrix} 0 & -\dfrac{1}{2}\left(\dfrac{\partial U}{\partial y}-\dfrac{\partial V}{\partial x}\right) & -\dfrac{1}{2}\left(\dfrac{\partial U}{\partial z}-\dfrac{\partial W}{\partial x}\right) \\[2mm] -\dfrac{1}{2}\left(\dfrac{\partial U}{\partial y}-\dfrac{\partial V}{\partial x}\right) & 0 & -\dfrac{1}{2}\left(\dfrac{\partial V}{\partial z}-\dfrac{\partial W}{\partial y}\right) \\[2mm] -\dfrac{1}{2}\left(\dfrac{\partial U}{\partial z}-\dfrac{\partial W}{\partial x}\right) & -\dfrac{1}{2}\left(\dfrac{\partial V}{\partial z}-\dfrac{\partial W}{\partial y}\right) & 0 \end{bmatrix} \tag{1}$$

In above equation the first item is rate-of-strain tensor represented by S, the second item is vorticity tensor represented by Ω [7]. The velocity gradient tensor ∇U can be presented as: $\nabla U = U_{ij} = S_{ij} + \Omega_{ij}$,

$$S_{ij} = \frac{1}{2}\left(\frac{\partial U_j}{\partial x_i}+\frac{\partial U_i}{\partial x_j}\right), \quad \Omega_{ij} = \frac{1}{2}\left(\frac{\partial U_j}{\partial x_i}-\frac{\partial U_i}{\partial x_j}\right). \tag{2}$$

The reference [8] defines the characteristic equation of velocity gradient tensor ∇U:

$$\lambda^3 + P\lambda^2 + Q\lambda + R = 0 . \tag{3}$$

The first invariant is $P = -\dfrac{\partial U_i}{\partial x_i}$, the second invariant is $Q = \dfrac{1}{2}\left(\dfrac{\partial U_i}{\partial x_i}\dfrac{\partial U_j}{\partial x_j}-\dfrac{\partial U_i}{\partial x_j}\dfrac{\partial U_j}{\partial x_i}\right)$, the third invariant $R = -\det\left(\dfrac{\partial U_i}{\partial x_j}\right)$ (det means determinant).

3.2. Q criteria

Fluid viscous resistance, baroclinity and earth Coriolis force are three main factors that generate vortex. The vortex isn't local phenomenon in time and space, but in fact some local characteristics can be used to evaluate the overall characteristics of vortex in realistic applications. The Q criteria which connects the second invariant Q of velocity gradient tensor with vortex was proposed for identifying vortex under incompressible or low-pressure conditions [9]. Some engineering applications always see the low-pressure as the mark of vortex, because fluid rotation generates centrifugal force which achieves balance with pressure, to create a low-pressure area at vortex center.

According to reference [10] and mass conservation equation: $\dfrac{\partial U}{\partial x}+\dfrac{\partial V}{\partial y}+\dfrac{\partial W}{\partial z}=\dfrac{\partial U_i}{\partial x_i}=0$, thus the first invariant $P=0$, so:

$$Q = \frac{1}{2}\left(\frac{\partial U_i}{\partial x_i}\frac{\partial U_j}{\partial x_j}-\frac{\partial U_i}{\partial x_j}\frac{\partial U_j}{\partial x_i}\right) = -\frac{1}{2}\frac{\partial U_i}{\partial x_j}\frac{\partial U_j}{\partial x_i} = -\frac{1}{2}\left(\Omega_{ij}\Omega_{ij}-S_{ij}S_{ij}\right) \tag{4}$$

3.3. Δ criteria

According to reference [11], if the eigenvalue $\lambda_1, \lambda_2, \lambda_3$ are real numbers the streamlines will not have center point on characteristic-plane. For incompressible flow, the possible condition which causes the percentage of vorticity tensor higher than strain tensor in flow transformations under Q criteria is:

$\Delta = \left(\dfrac{Q}{3}\right)^3 + \left(\dfrac{R}{2}\right)^2 > 0$. Q, R are the second, third invariants of velocity gradient tensor.

3.4. λ_{ci} criteria

λ_{ci} criteria are based on Δ criteria, when $\Delta > 0$ the characteristic equation has one real root γ_1, two conjugate imaginary roots γ_2 and γ_3, so: $\gamma_1 = \lambda_r$, $\gamma_2 = \lambda_{cr} + i\lambda_{ci}$, $\gamma_3 = \lambda_{cr} - i\lambda_{ci}$

Set: $\xi_1 = \sqrt[3]{\sqrt{\Delta} - \dfrac{R}{2}}$, $\xi_2 = \sqrt[3]{\sqrt{\Delta} + \dfrac{R}{2}}$, solving simple cubic equation, so: $\lambda_{ci} = \dfrac{\xi_1 + \xi_2}{2}\sqrt{3}$. Investigating if $\lambda_{ci}^2 > 0$ to estimate the existence of vortex and judging vortex rotational direction based on the plus or minus of vorticity.

3.5. λ_2 criteria

λ_2 criteria proposes that the vortex center pressure is lowest while ignoring the influences of unstable stress and viscosity. The conditions are the three eigenvalues of symmetric tensor to have: $\lambda_1 \leq \lambda_2 \leq \lambda_3$, and $\lambda_2 < 0$. Q criteria can look for the domains where vorticity tensor higher than strain tensor, and λ_2 criteria can only do it on specific planes.

4. Comparisons of vortex identification algorithms

Vortex identification comparisons are shown in Figure 3. The vortex identification methods based on the second invariant Q decomposed from velocity gradient tensor, the characteristic equation discriminant Δ, the complex eigenvalue imaginary part λ_{ci} and the pressure second eigenvalue λ_2 further weaken the influence of pure-shear on vortex identification. The identified vortex area (Figure 3 (a)-(d)) is much smaller than traditional vorticity method (Figure 3 (e)) and shows clearer vortex formations.
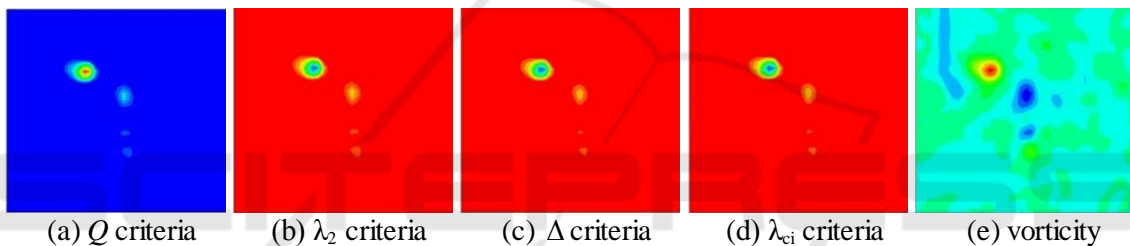

(a) Q criteria   (b) λ_2 criteria   (c) Δ criteria   (d) λ_{ci} criteria   (e) vorticity

Figure 3. Comparison of traditional vortex identification criteria based on flapping wing aircraft.

By comparing the above graphs, we can see that the Δ criteria further reduces the influence of pure shear flow on vortex identification relative to other criteria (see Figure 3 (e)). The purpose of this paper is to study the application of vortex identification algorithm. The key lies in mastering the whole process of PIV data post-processing. Therefore, the Δ criteria is selected as the criteria for the analysis of Aircraft wake vortices and four-vortex systems.

5. Applications of vortex identification algorithms

5.1. Aircraft wake vortex visualization

Figure 4-Figure 7 are wake vortex visualizations based on wake vortex data. Figure 4 is 3D track figure of single-vortex center. Extracting Δ value from single-vortex data obtained in PIV experiments to be vortex center. Figure 4. shows the motion trail of wake vortex and position mutation of vortex center due to small disturbance but not presents the strength transformations of wake vortex.

Figure 5 is 3D track figure of a twin-vortex system which indicates the 8 cross sections of twin-vortex trail motions. The blue isoclines show the twin-vortex motions while Δ as minus, the red dotted lines show the trails of twin-vortex centers. Figure 5 presents the twin-vortex twist under R-L instability, but Δ criteria can't tell the direction of main vortex and secondary vortex and unable to identify them.

Figure 6 is 4D figure of tangential velocity of twin vortices. Extreme points of Δ create a waterline, extracting tangential velocity of all points of it to make the figure with 18 sets of data.
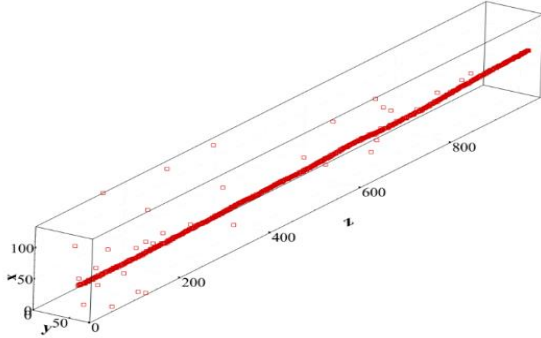

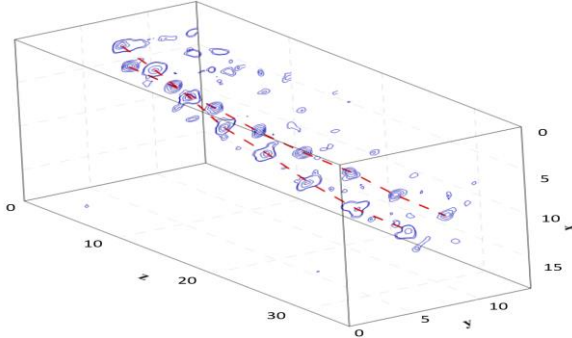**Figure 4.** 3D track figure of single-vortex center.

Figure 5. 3D track figure of twin-vortex system.

Vortex core is within-area where tangential velocity is highest [12]. In Figure 6. the vortex core energy is relatively concentrated as two vortices generated, energy peak shown in darkest colour; the primary vortex interacts with secondary vortex and transmits energy quickly to other areas thus weakens vortex core energy till dissipation.
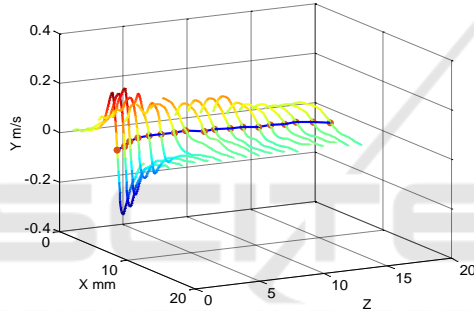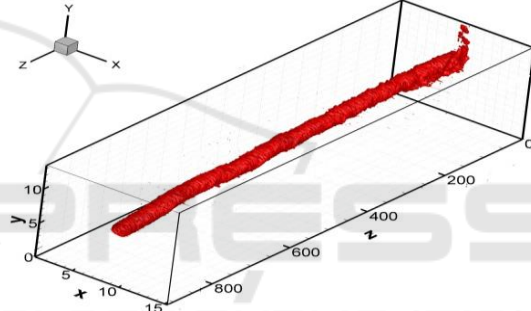

Figure 6. 4D figure of tangential velocity.

Figure 7. 3D track figure of single vortex-tube.

Creation method of Figure 7 is similar to Figure 5., overlapping series of contour surfaces based on PIV experimental data to form 3D vortex-tube figure. Figure 7 not only clearly presents the wake vortex motion track but also exhibits the vortex-tube energy change according to vortex-tube position and size. As Figure 7 indicates, at the first beginning vortex-tube motion track is linear, the wake vortex formations basically unchanged; vortex formations start to have twist due to long wave instability which causes shear-led vortex core energy dissipation but still maintain basically linear.

5.2. 4-vortex system identification

This paper applies Δ criteria to a wake 4-vortex system to study the influence of initial position & strength of secondary vortex on main wake vortex dissipation with flow visualization analysis to better understand flow mechanism. The PIV experimental sets are shown in Table 1 and Table 2.

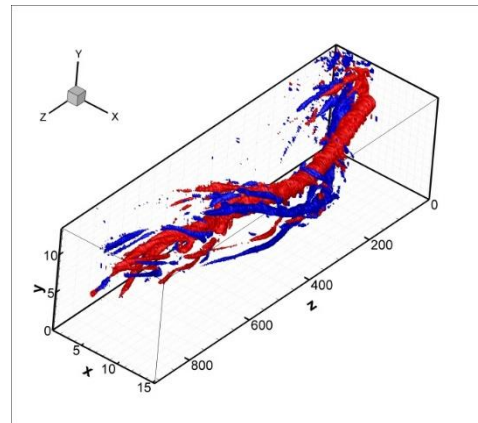**Table 1.** Initial position sets of secondary vortex.

Experiment NO.	Angle of attack (Main wing)	Angle of attack (Small wing)	Distance
A	10°	6°	40mm
B	10°	6°	45mm
C	10°	6°	50mm

Table 2. Initial strength sets of secondary vortex.

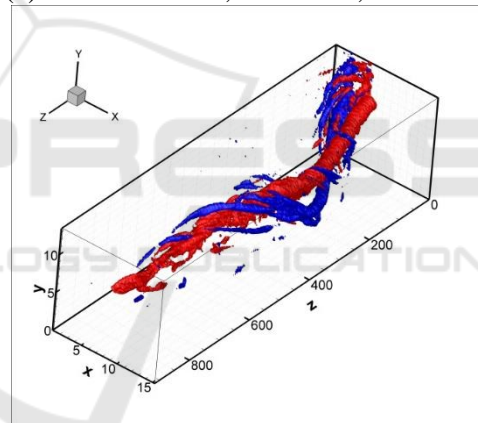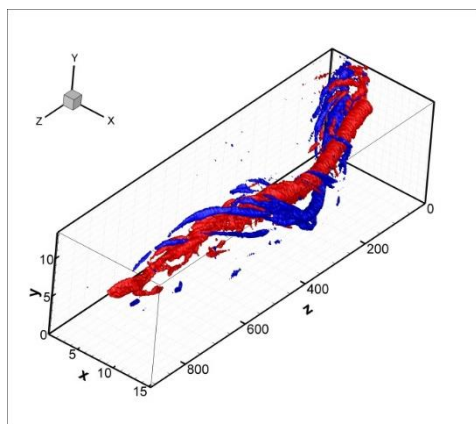| Experiment NO.	Angle of attack (Main wing)	Angle of attack (Small wing)	Distance
D	10°	4°	50mm
C	10°	6°	50mm
E	10°	8°	50mm
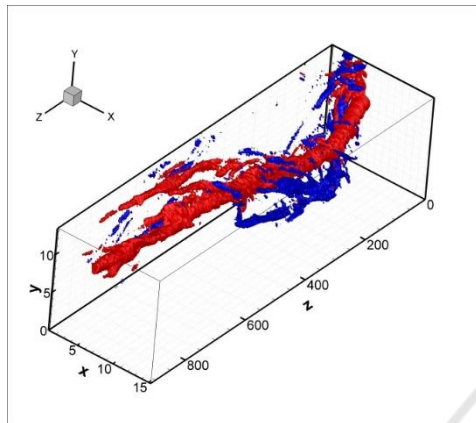
(a) A: M.A.A. 10°, S.A.A. 6°, D 40mm
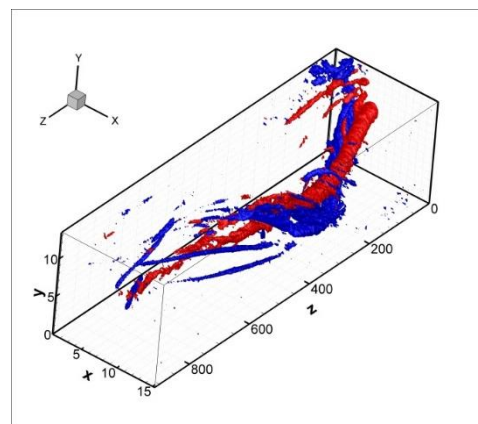
(b) D: M.A.A. 10°, S.A.A. 4°, D 50mm
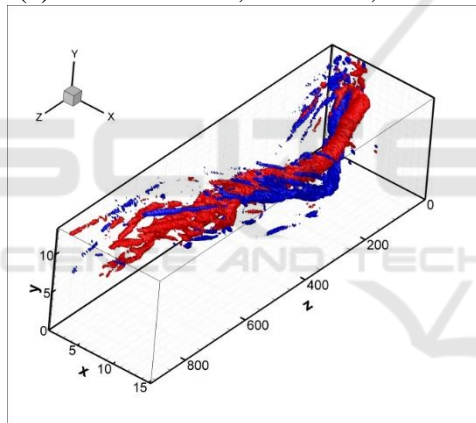
(c) B: M.A.A. 10°, S.A.A. 6°, D 45mm

(d) C: M.A.A. 10°, S.A.A. 6°, D 50mm

(e) C: M.A.A. 10°, S.A.A. 6°, D 50mm

(f) E: M.A.A. 10°, S.A.A. 8°, D 50mm

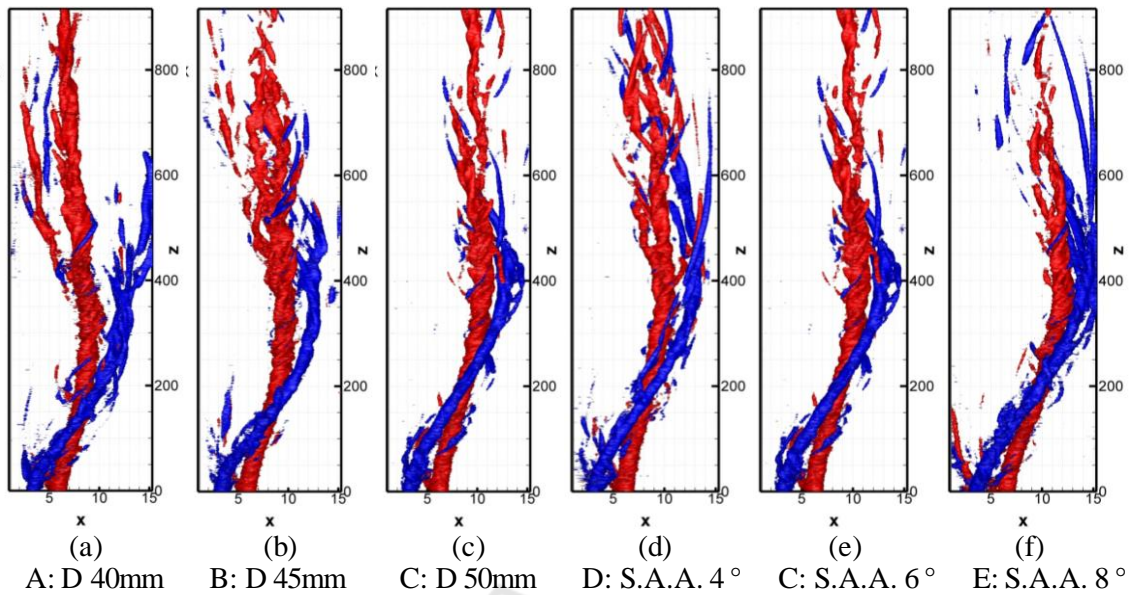**Figure 8.** Twin-vortex formations under various experimental sets.

(a)	(b)	(c)	(d)	(e)	(f)
A: D 40mm	B: D 45mm	C: D 50mm	D: S.A.A. 4°	C: S.A.A. 6°	E: S.A.A. 8°

Figure 9. Twin-vortex x-z views under various experimental sets.

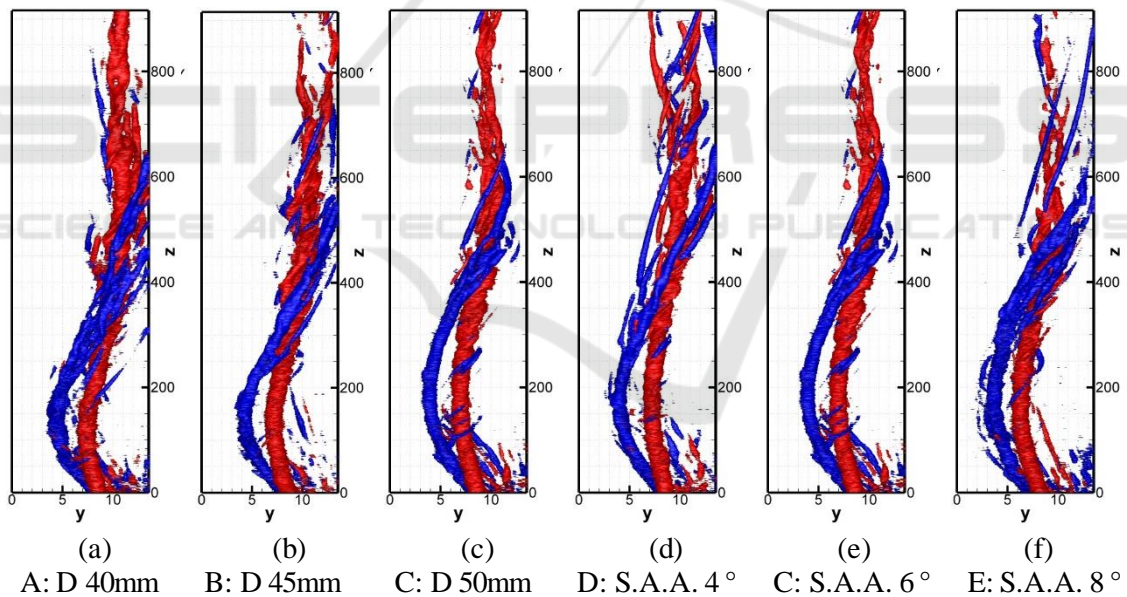| (a)	(b)	(c)	(d)	(e)	(f)
A: D 40mm	B: D 45mm	C: D 50mm	D: S.A.A. 4°	C: S.A.A. 6°	E: S.A.A. 8°

Figure 10. Twin-vortex y-z views under various experimental sets.

In experimental sets A, Figure 9 (a) shows that the secondary vortex has been thrown off due to smaller distance during process of stripping effect. Figure 8 (c) (Sets B with proper distance) indicates the trend that secondary vortex is induced to rotate around main vortex under Rayleigh-Ludwieg instability influence [13]. Experiment C (Figure 9 (c), Figure 10 (c)) has max twin-wing distance, the main vortex and secondary vortex interact lately then vortex core breaks while dissipating energy.

Processing PIV velocity field data of experiments (D, C, E) to study the strength relations between main vortex and secondary vortex. Figure 9 (d), (e), (f) have the similar main vortex tube

shapes but secondary vortex tube sizes up as its strength (angle of attack) increases under same twin-wing distance. As shown in Figure 10 (d), (f), the main vortex strength is not obviously weakened by secondary vortex in experiment D but greatly weakened in experiment E thus reveals that stronger secondary vortex will speed up main vortex dissipation. Figure 9, Figure 10 also shows that the drift distance and twist deformations triggered by twin-vortex interactions increase as secondary vortex strength up.

In order to distinguish the spatial development of the main vortex and the secondary vortex, we define the red represents anticlockwise main vortex (positive), the blue represents clockwise secondary vortex (negative). The magnitude of the vorticity cannot be inferred directly from the colour of the vortex contour. The specific comparison requires the use of circumstantial analysis.

The Γ_2/Γ_1 is the ratio of secondary vortex initial circulation to main vortex initial circulation, η is the attenuation rate of main vortex circulation. Performing correlation analysis to the first image, the vorticity less than zero is added together to obtain Γ_2, and the vorticity greater than zero is added to obtain Γ_1. (Table 3).

Table 3. Main vortex vorticity attenuation.

Experiment	Γ_2/Γ_1	Distance	η (%)
A	-0.68	40mm	23.8
B	-0.68	45mm	24.4
C	-0.68	50mm	20.7
D	-0.54	50mm	18
E	-0.88	50mm	21.7

According to Table 3., the experiment B has the biggest attenuation rate, which reveals that there is an ideal distance to achieve the best dissipation effect as angle of attack kept same. While twin-wing distance and main wing attack angle kept same, the secondary wing attack angle increases will cause stronger secondary vortex which speeds up dissipation. However, for real flight conditions, the small wing hardly generates strong-enough vortex that can effectively influence dissipation. So choosing the optimal distance and secondary wing attack angle should be best way to dissipate vortex energy.

6. Conclusions

This paper focuses on research of local vortex identification methods of the second invariant Q, the characteristic equation discriminant Δ, the complex eigenvalue imaginary part λ_{ci} and the pressure second eigenvalue λ_2 which are deduced with velocity gradient tensor ∇U. The main conclusions are as follow:

1. Q criteria, Δ criteria, λ_2 criteria and λ_{ci} criteria are equivalent under incompressible conditions;

2. Q criteria and λ_2 criteria are equivalent, Δ criteria and λ_{ci} criteria are equivalent under 2D conditions while zero threshold as vortex boundary;

3. Q criteria, Δ criteria, λ_2 criteria, and λ_{ci} criteria have basically same results of identifying vortex center positions and vortex core sizes while non-zero threshold as vortex boundary;

4. Δ criteria is more suitable for data processing because it can further weaken influence of pure-shear flow.

Wake vortex visualizations based on identification methods (programmed in Matlab & Tecplot) clearly exhibit the vortex center track, vortex core size and vortex domain, which help to better understand interactions & dissipation of wake vortices. Vortex-tube visualizations are made to study the influence of original circulations & positions of twin-vortex on wake vortex dissipation. Conclusions revealed by visualizations:

5. Secondary vortex with stronger circulation will speed up main vortex dissipation;

6. Secondary vortex with appropriate circulation will lead to minimum wake vortex strength;
7. The smaller twin-vortex distance will make 2 vortices interact earlier.

References

[1] Raffel, M. et al., Post-Processing of PIV Data. Particle Image Velocimetry, pp.177–208.

[2] Simoni, D., Lengani, D. & Guida, R., 2016. A wavelet-based intermittency detection technique from PIV investigations in transitional boundary layers. Experiments in Fluids, 57(9).

[3] Camussi, R., 2002. Coherent structure identification from wavelet analysis of particle image velocimetry data. Experiments in Fluids, 32(1), pp.76–86.

[4] Kolář, V., 2007. Vortex identification: New requirements and limitations. International Journal of Heat and Fluid Flow, 28(4), pp.638–652.

[5] Majda, A.J. & Bertozzi, A.L., Computational Vortex Methods. Vorticity and Incompressible Flow, pp.190–255.

[6] Alekseenko, S.V., Kuibin, P.A. & Okulov, V.L., Equations and laws of vortex motion. Theory of Concentrated Vortices, pp.9–68.

[7] Liu, C. et al., 2016. New omega vortex identification method. Science China Physics, Mechanics & Astronomy, 59(8).

[8] Epps, B., 2017. Review of Vortex Identification Methods. 55th AIAA Aerospace Sciences Meeting.

[9] Kolář, V., Moses, P. & Šístek, J., 2011. Triple Decomposition Method for Vortex Identification in Two-Dimensional and Three-Dimensional Flows. Computational Fluid Dynamics 2010, pp.225–231.

[10] Bao, F. et al., 2014. An Investigation on the Lift Mechanism of Flapping-Wing Air Vehicle. Advanced Materials Research, 971-973, pp.353–358.

[11] Bao Feng, Liu Jinsheng, Zhu Rui, et al. 2015. Experimental Study of Aircraft Tail Vortical Rayleigh-Ludwieg Instability[J].Acta Aeronautica et Astronautica Sinica, 2166-2176.

[12] Carmer, C.F. v. et al., 2008. Identification of vortex pairs in aircraft wakes from sectional velocity data. Experiments in Fluids, 44(3), pp.367–380.

[13] Kolář, V., Moses, P. & Šístek, J., 2011. Triple Decomposition Method for Vortex Identification in Two-Dimensional and Three-Dimensional Flows. Computational Fluid Dynamics 2010, pp.225–231.